Control of germanium diffusion using low quantities of co-implanted silicon isotopes

NELIS, ADRIEN; Barba, David; Terwagne, Guy

Published in:
Journal of Applied Physics

DOI:
10.1063/5.0020368

Publication date:
2020

Document Version
Publisher's PDF, also known as Version of record

Journal of Applied Physics

Control of germanium diffusion using low quantities of co-implanted silicon isotopes

Cite as: J. Appl. Phys. **128**, 125705 (2020); https://doi.org/10.1063/5.0020368
Submitted: 30 June 2020 . Accepted: 30 August 2020 . Published Online: 23 September 2020

A. Nélis, D. Barba, and G. Terwagne

Journal of Applied Physics ARTICLE scitation.org/journal/jap

Control of germanium diffusion using low quantities of co-implanted silicon isotopes

Cite as: J. Appl. Phys. **128**, 125705 (2020); doi: 10.1063/5.0020368
Submitted: 30 June 2020 · Accepted: 30 August 2020 ·
Published Online: 23 September 2020

A. Nélis,[1,a)] D. Barba,[2] and G. Terwagne[1]

AFFILIATIONS

[1]LARN, Namur Institute of Structured Matter (NISM), University of Namur (UNAMUR), B-5000 Namur, Belgium
[2]INRS-EMT, 1650 boul. Lionel-Boulet, Varennes, Québec J3X 1S2, Canada

[a)]**Author to whom correspondence should be addressed:** adrien.nelis@unamur.be

ABSTRACT

The thermal diffusion of Ge implanted into SiO_2 films growth on a Si substrate has been studied by nuclear analyses and μ-Raman spectroscopy with and without the presence of co-implanted ^{30}Si and ^{29}Si barriers, each located from both sides of the Ge implanted distribution. Combination of Rutherford backscattering spectroscopy and Resonant nuclear reaction analysis shows that, under thermal activation at 1100°C, implanted Ge diffuses differently toward the sample surface and the SiO_2/Si interface due to the occurrence of Ge outgassing effects, as well as the non-homogenous distributions of the implanted ion species and the defects they have generated inside SiO_2. A maximum local atom concentration of co-implanted silicon as low as ∼1.6 at. % is found to completely block the germanium diffusion in both directions, leading to the formation of Ge nanocrystals and Si/Ge aggregates evidenced by μ-Raman spectroscopy. In addition to highlighting the role of Si excess on the Ge trapping mechanism, such a result makes the nominal silicon oxide stoichiometry and composition two crucial parameters to stabilize Ge during high temperature annealing, which explains the strong discrepancies reported for the Ge thermal diffusion coefficient in the literature.

I. INTRODUCTION

Research in the field of group IV semiconductors has been of great interest during the last few decades for their applications in memory devices, nanoelectronic or optoelectronic, as photovoltaic (PV) cells.[1–3] Germanium is a good candidate thanks to a very low energy bandgap, large absorption in the visible range, and an adaptability to silicon-based industry due to a similar atomic structure.

Semiconductor nanocrystals, integrated into dielectric layers by ion implantation, offer new possibilities thanks to manifold associated optoelectronic properties. Their tunable bandgap and the potential activation of multiple exciton generation (MEG) can greatly improve energy conversion in PV cells. This enhanced photovoltaic efficiency strongly depends on the size of the nanocrystals and their depth-distribution inside the dielectric layer.[1–5]

Controlling the nanocrystal distribution, size, and purity is a great challenge to tune their physical properties for specific applications. The co-implantation of silicon excess was found to be an efficient solution to annihilate the Ge thermal diffusion for temperatures as high as 1000–1100 °C[6–12] and thus control the Ge nanocrystal (Ge-ncs) depth-distribution after annealing. It has been shown that the production of silicon excess using this technique can reduce the long-range redistribution of implanted Ge during high temperature annealing[5] and annihilate its release from the fused silica or thermally grown SiO_2 oxide matrices.

In this work, both the diffusion of Ge atoms implanted into a thermally grown SiO_2 layer and the diffusion barrier effect of co-implanted ^{30}Si and ^{29}Si isotopes are investigated by Rutherford Backscattering Spectroscopy (RBS) and Resonant Nuclear Reaction Analysis (RNRA) measurements.

The highly asymmetric upward and downward diffusion of the Ge nominally implanted in the middle of the SiO_2 layer is evidenced by RBS/RNRA, showing an accumulation of Ge after thermal annealing, within the sample regions where both the concentration of implanted Ge and the ion damaging are maximum. The role played by the ion-induced depth-dependent structural and composition changes on the Ge diffusion mechanism is discussed by comparing the profiles of Ge-implanted samples to those recorded for Ge thin layers embedded in SiO_2/Si systems, prepared by thermal evaporation and physical vapor deposition (PVD).

When the implanted Ge is sandwiched between two Si co-implanted sublayers, both the diffusion toward the sample surface and the SiO_2/Si interface are blocked. In order to distinguish the effects related to the blocking of diffusing Ge by the upper and lower Si barriers, two different ^{30}Si and ^{29}Si isotopes were implanted into the top and bottom parts of the SiO_2 layer, respectively. Whereas the diffusion barrier effect becomes effective for low fluences of co-implanted Si and complete for implanted Si-excess of 1.6 at. % at maximum, a continuous growth of the Ge nanocrystallites is observed by μ-Raman upon Si co-implantation. This Ge-ncs nucleation is accompanied by one of the Si–Ge chemical bonds, suggesting that the local reduction of the Ge thermal coefficient evidenced by RBS/RNRA results from enhanced Si/Ge chemical trapping effects and Ge nanoclustering in the ion-damaged sublayers. These features can be explained from the different effects that contribute to the thermal diffusion mechanism, which are discussed here to describe both the RBS/RNRA and μ-Raman measurements.

II. EXPERIMENT

300 nm thick wet-oxidized (100) silicon wafers were implanted with $^{30}Si^-$ prior to $^{29}Si^+$ ions at energies of 35 and 170 keV, respectively, and fluences varying from 1 to 8×10^{16} Si/cm^2. Projected ranges of $^{30}Si^-$ and $^{29}Si^+$ in SiO_2 are around 20 and 275 nm, respectively (depending on implantation fluences). $^{74}Ge^+$ ions were later implanted with a single energy of 230 keV in order to obtain a main depth around the middle of the SiO_2 layer. A $^{74}Ge^+$ fluence varying from 6×10^{16} to 2.5×10^{17} ^{74}Ge/cm^2 has been used. All implantations were performed with ALTAÏS (Accelerateur Linéaire Tandetron pour l'Analyse et l'Implantation des Solides) and the 2 MV Tandetron accelerator installed at LARN (UNamur). SRIM–TRIM (Stopping and Range of Ions in Matter–TRansport of Ions in Matter[16]) calculations have been used to calculate projected ranges taking account of surface sputtering and swelling effects, considering a sputtering yield of 0.85 at./Ge.

After implantation, all samples were annealed inside a quartz tube furnace heated at 1100 °C for 60 min under an ultrahigh purity nitrogen (N_2) environment, using a gas purifier and a hermetic setup to limit contamination and oxidation from air ambient. Annealing was performed with the facilities installed at the INRS-EMT center (Varennes, Québec) and at LARN (UNamur).

The fluences and depth-profiles of implanted Ge ions and Si isotopes were measured by RBS, using 2 and 3 MeV $^4He^+$ beams for two scattering angles (165 and 170°). The choice of 3 MeV alpha beam is justified by the mass resolution observed for the subsurface implanted ^{30}Si ions. RBS data were treated using SIMNRA[29] (combined with SimTarget, developed by J.L. Colaux[36]) and DataFurnace[30] (NDF) programs.

^{30}Si and ^{29}Si depth-profiles were measured by using $^{29}Si(p,\gamma)^{30}P$ and $^{30}Si(p,\gamma)^{31}P$ narrow resonant reactions, around 414 and 620 keV, respectively,[17] into a low-background system coupled with a NaI(Tl) well detector installed on ALTAÏS. γ-rays are detected in energy windows (4–6 MeV for $^{29}Si(p,\gamma)^{30}P$ and 3.5–9.5 MeV for $^{30}Si(p,\gamma)^{31}P$) given in Ref. 17.

PVD depositions and thermal evaporation were performed into a vacuum chamber. Samples are made in three successive steps without breaking vacuum : (1) SiO_2 plasma deposition using a silicon cathode submitted to a reactive atmosphere composed of Ar with 5 sccm of O_2, (2) thermal evaporation of natural germanium powder under vacuum (10^{-4} Pa) with a deposition rate of 1 Å/s, and (3) SiO_2 deposition under the same conditions than step 1.

μ-Raman measurements were performed using a confocal Renishaw RM 3000 spectrometer equipped with a digital camera, a ×50 objective lens of 0.75 numerical aperture, and a 514 nm laser probe.

III. IMPLANTATION DEPTH-PROFILES

Powerful ion beam analysis (IBA) techniques are used to highlight the implantation profiles. Figure 1(a) shows the result of a 3 MeV alpha particles RBS spectra of a triply implanted sample, i.e., with two silicon implantations followed by a single germanium implantation. In this configuration, Ge implantation will always be localized at the same projected range. In Fig. 1(a), the germanium peak (at high energies) and subsurface implanted ^{30}Si atoms can easily be fitted on RBS spectra. This last one is well untied from Si-contained SiO_2 signal, thanks to a good mass resolution at 3 MeV. ^{29}Si contribution is less obvious to highlight owing to peak drowning into a substrate signal. This issue justifies the use of isotope sensitive analysis techniques, such as RNRA.[37,38]

In addition to being isotopically sensitive, the depth resolution is better for RNRA than RBS,[32] as described in Ref. 31. For backscattering analysis, the depth resolution is essentially ruled by the energy resolution of the detector (Passivated Implanted Planar Silicon), which is typically around 15 keV for Si-based PIPS detectors. For resonance profiling, depth resolution is mainly controlled by the energy spread of the incident beam (∼hundreds of eV) and by the resonance width (<100 eV in our cases).[17] An example of the evolution of RNRA depth resolution is shown in Fig. 1 of Ref. 38.

Weak percentages of ^{29}Si and ^{30}Si contained in natural silicon (^{28}Si : 92.2%; ^{29}Si : 4.7%; ^{30}Si : 3.1%) allow us to bring out implanted species by RNRA measurements. Figures 1(b) and 1(c) illustrate, respectively, depth-profiles of ^{29}Si and ^{30}Si isotopes obtained using $^{29}Si(p,\gamma)^{30}P$ and $^{30}Si(p,\gamma)^{31}P$ reactions (open squares). In Fig. 1(c), RNRA measurements are in good agreement with RBS fitted profiles (black dots). The RNRA data obtained by $^{29}Si(p,\gamma)^{30}P$ [Fig. 1(b)] were used to adjust the fit of the ^{29}Si peak in RBS spectra.

RNRA raw data [$Y(E_0)$], which are a convolution of the beam energy spread, the straggling function, and the resonance width [all included in $F(E_0, x)$], are deconvoluted using the Vavlov program developed at LARN,[28]

$$Y(E_0) = \int_0^x c(x)F(E_0, x)dx, \quad (1)$$

where $c(x)$ is the concentration depth-profile and $x = \frac{E_0 - E_R}{S_{E_R}}$ with S_{E_R} being the stopping power and E_0 and E_R being the induced and resonant energies, respectively. The Vavlov program enables us to get the concentration profile $c(x)$ as a function of depth (described in Refs. 28, 37, and 38).

Combination of both techniques, RBS and RNRA, allows us to completely define the three implantation profiles of $^{29}Si^+$, $^{30}Si^-$, and $^{74}Ge^+$.

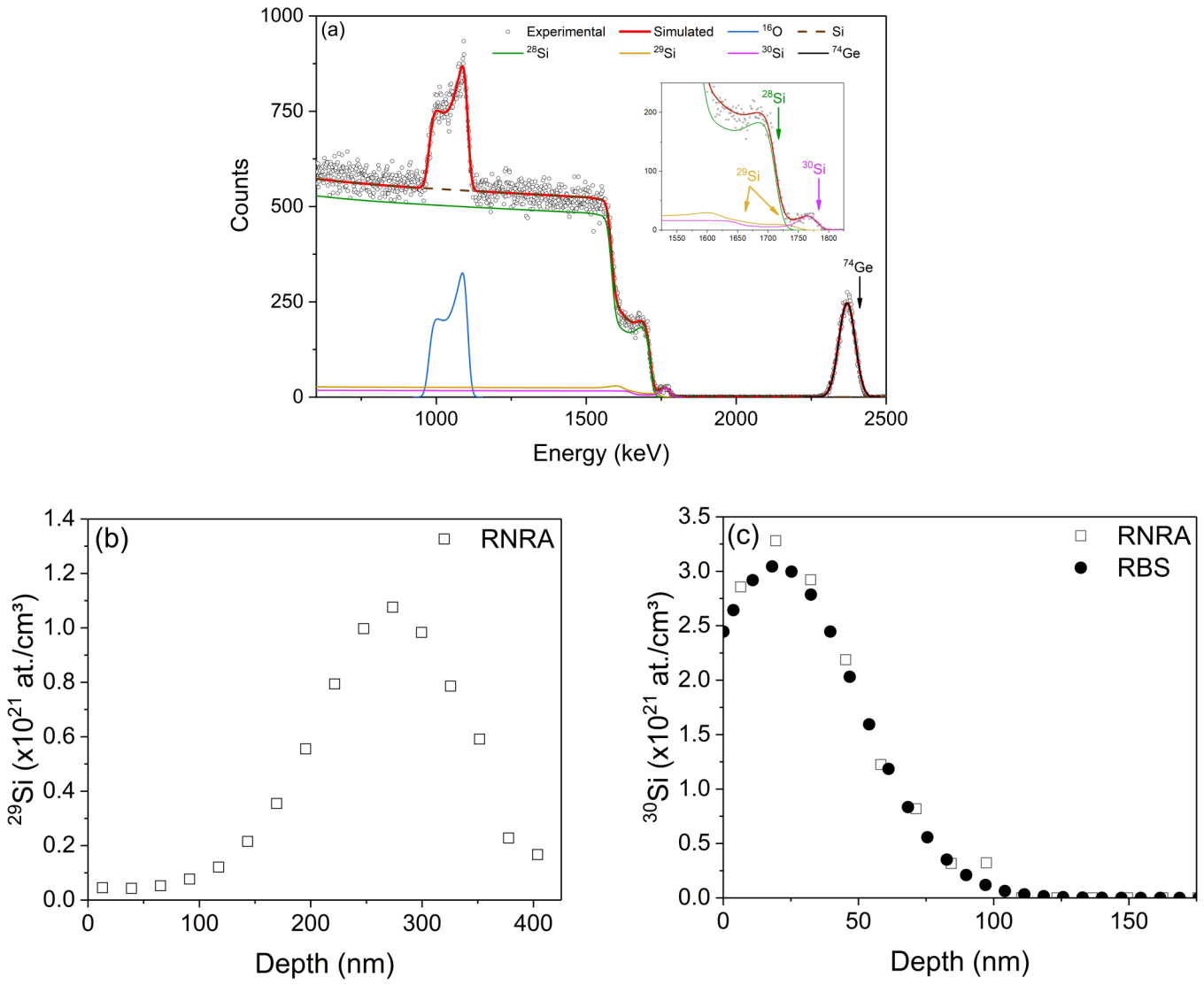

FIG. 1. (a) RBS analysis of a 8×10^{16} $^{74}Ge/cm^2$ implanted sample, co-implanted with 2×10^{16} Si/cm^2 on either side of Ge, where ^{30}Si is well untied from the substrate signal with a maximum about 1767 keV. RNRA extracted using the Vavlov program for ^{29}Si (b) and ^{30}Si (+ RBS) (c) for the same sample.

IV. RESULTS AND DISCUSSION

A. Anisotropic thermal diffusion of Ge

Figure 2 shows the germanium depth-profile obtained by RBS in a sample implanted solely with a measured fluence of 6×10^{16} $^{74}Ge/cm^2$, before and after 1 h annealing. The "as implanted" profile (blue dots) is consistent with SRIM–TRIM simulations (black solid line), taking into account interactions between the energetic ions and the substrate, with an eroded SiO_2 thickness of ~10 nm. The origin of the x axis corresponds to the sample surface (through which the Ge ions have penetrated) and the right part to the silicon substrate whose SiO_2/Si interface is located 295 nm below the surface.

As shown in previous works,[5–7] an important thermal diffusion of Ge is observed in both directions. After annealing, the Ge depth-profile exhibits two peaks of the Gaussian shape. This migration is highly asymmetric with a major peak (peak 1) centered at a depth of 140 nm, which is shifted upward by about 15 nm with respect to the center of the as-implanted depth-distribution. The second peak (peak 2) is located at the SiO_2/Si interface, where diffusing Ge has accumulated (red crosses). These features are consistent with the RBS measurements obtained by Minke and Jackson and Markvitz *et al.* in thermal SiO_2 fused and crystallized silica, who also found that the diffusing Ge accumulates in the vicinity of the sample surface[6,7] and at

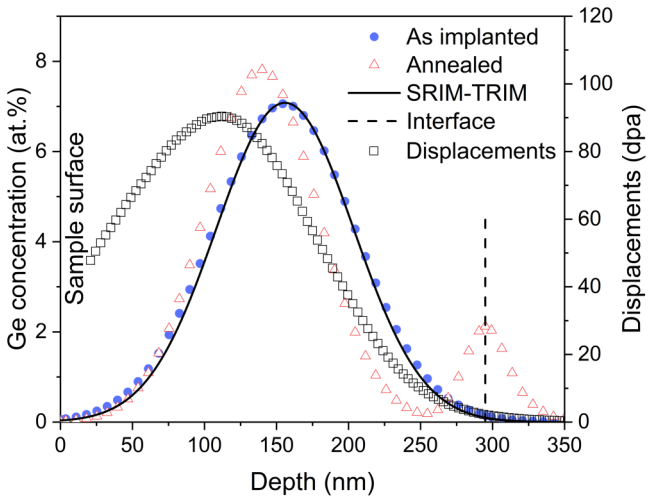

FIG. 2. Fitting curves of RBS analyses of germanium depth-profile evolution before (blue dots) and after (red crosses) 1 h annealing at 1100 °C for a sample not co-implanted with Si, supported by SRIM–TRIM calculations. Displacements (calculated from TRIM simulation) are represented by open squares (right y axis).

the SiO_2/Si interface.[7] Contrary to fused silica implanted with Ge and annealed above 900 °C,[9–11,14] no drastic outgassing-like comportment is reported. As measured by RBS, less than 4% of germanium loss is measured, which is consistent with the ones we have measured in other thermally grown silicon oxides.[4,5]

In Fig. 2, the Ge that migrated upward during annealing is found to accumulate in the region where most the defects generated by the Ge implantation are located. On the other hand, about 11.5% of the total amount of Ge is observed at the SiO_2/Si interface after thermal activation. This asymmetric shape along the sample depth of the Ge distribution after annealing results from the combination of three factors: (1) the composition and geometry of the implanted medium, which is highly anisotropic, (2) the influence of oxygen, and (3) the trapping of diffusing germanium through the formation of Ge–Si and Ge–Ge chemical bonds.

(1) The layer anisotropy results from the as implanted germanium depth-profile, which is located around the center of the SiO_2 layer, as measured by RBS (blue dots in Fig. 2), the depth-distribution of implantation-induced damage, which is maximal between the surface and the Ge projected range (represented by open squares in Fig. 2 and calculated by SRIM–TRIM),[16] and the nature of the implanted medium: a 300 nm homogeneous SiO_2 layer edged by SiO_2/Si and gas/SiO_2 interfaces. The combination of these three contributions makes the composition, density, and atom ordering of the studied samples non-uniform in depth.

(2) As stated by the results published in the literature,[7,8,11,12,18,19] Ge atoms were found to link with O inside SiO_2 layers after implantation,[27] as a side effect of irradiation damages or during annealing, to form gaseous GeO. With the GeO density being smaller than that of air, Ge migration is favored toward the sample surface. This oxygen has two possible origins: it can come from residual moistures present in the annealing atmosphere or from the oxide itself and released by the damages induced by implantation. In this study, thermal processes are performed under ultrahigh purity atmosphere; thus, atmosphere contribution is limited, and we consider that oxygen mostly comes from the SiO_2 matrix.

(3) Finally, the chemical trapping effect evidenced in similar systems has shown that the diffusion of germanium is strongly affected by the formation of Ge–Si and Ge–Ge bonds, leading to nanoclustering and blocking barrier effects.[5,13–15]

In agreement with the models proposed to describe the Ge diffusion mechanism inside SiO_2, we infer that the Ge implanted should preferentially diffuse upward and its motion would be affected by the nature of crossed medium. Such a scenario is supported by the data reported in Fig. 2, where the region containing the greatest concentration of Ge after annealing (peak 1) corresponds to the region where Ge atoms have greater probability to nucleate, and the accumulation of Ge found at the SiO_2/Si interface (peak 2) is a direct consequence of the Si/Ge trapping.[5,14,15] This SiO_2/Si interface is known to release SiO molecules that react with GeO through the following reaction:[34]

$$GeO + SiO \rightarrow Ge + SiO_2, \quad (2)$$

as confirmed by XPS measurements showing the formation of Ge–Ge and Ge–Si chemical bonds.[12,27] However, it was evidenced by Markvitz *et al.* using transmission electron microscopy (TEM) investigations that the formation of such bonds would not necessary lead to the nucleation of Ge.[7]

The trapping effect is less dominant in the subsurface region where Ge is close to the gas/SiO_2 interface. This allows low quantities of highly volatile GeO to desorb through the surface.

Despite the presence of strong material density variations originating from recoiled Si and O target atoms,[16] the structural defects generated by implantation are not responsible for the anisotropic Ge diffusion. This remark is consistent with previous works, highlighting the poor contribution of grain boundary diffusion and the cracking layer to the Ge displacement.[6] It is also consistent with the fact that most of the damage induced by ion implantation is restored for SiO_2 and silica films annealed at temperatures higher than 1000 °C[33] (not fully efficient at the high fluences used in this work). Hence, although the efficiency of this structural recovery process may differ in the different sample regions, the Ge diffusion mechanism appears to be mostly dominated by factors (2) and (3). This is confirmed by the thinning of peak 1 after annealing in Fig. 2, suggesting Si/Ge trapping and nanoclustering during the upward diffusion of Ge.

For fluences as high as 2.5×10^{17} $^{74}Ge/cm^2$, the density of defects is increased by factor 4, and the damage and Ge depth-profiles superimpose due to erosion (30 nm). In these conditions, peak 1 is measured to shift only by 4 nm with respect to the as implanted peak position, which is four times less than for 6×10^{16} $^{74}Ge/cm^2$, and ~9% of the total implanted Ge atoms accumulate at

the SiO_2/Si interface, confirming the participation of damage in Si/Ge trapping during Ge diffusion.

B. Ge diffusion through non-implanted SiO_2/Si samples

In order to highlight the significant role of implantation-induced effects discussed above on Ge diffusion, a sample free of ion damaging was prepared by thermal evaporation and plasma vapor deposition (PVD). This sample is composed of a thin germanium layer thermally evaporated inside a vacuum chamber (10^{-4} Pa). This evaporation step is inserted between two SiO_2 plasma depositions to obtain a germanium layer of about 15–20 nm thickness embedded into a homogeneous medium exempt of implanted ions and atoms displaced by collision with impinging ions.

Figure 3 shows the RBS spectra, measured before and after annealing, of non-implanted samples. Two samples were annealed at 1100 °C under pure nitrogen atmosphere for 30 and 60 min, respectively. After thermal treatment, the Ge is found to diffuse through the two deposited SiO_2 layers. The diffusion process occurs at the same rate upward and downward, leading to a final depth-distribution that is almost symmetric with respect to the Ge layer. In the absence of implantation, only a poor fraction of Ge atoms are supposed to be chemically bonded to oxygen to form highly volatile GeO responsible for upward diffusion. As for the Ge implanted sample shown in Fig. 2, a buildup of the Ge concentration is observed with the increase of the annealing time in the vicinity of the Si substrate, which can be attributed to Si/Ge trapping effects, resulting from the abrupt increase of the Si concentration. Nevertheless, in the absence of ion-induced effects within the first 50 nm of the sample, no accumulation of Ge is observed between the sample surface and the deposited Ge layer, resulting in 12%–13% of Ge outgassing. Such a behavior is consistent with the expected result since for the non-implanted samples, the Ge diffusing upward is not affected by the presence of local defects and excess atoms, which both reduce its displacement and contribute to its clustering.[5,13–15]

Using Fig. 3 and second Fick's law, we are able to calculate the diffusion coefficient of germanium in this deposited oxide, $D_{1100°C}$,

$$C(x,t) = \frac{C_0}{2\sqrt{D_{1100°C}t}} e^{-(x-x_0)/4D_{1100°C}t}, \quad (3)$$

with C_0 being the initial concentration (t = 0 s), x_0 the position of the distribution maximum, and t the annealing time. At 1100 °C, this coefficient is found to be $D_{1100°C} \sim 10^{-14}$ cm^2/s, which is several orders of magnitude higher than current coefficients referenced in the literature.[6,10] These coefficients are generally obtained on implanted samples whose diffusion is influenced by the three factors explained in Sec. IV A. The diffusion coefficient strongly depends on implantation and annealing conditions as well as the host matrix quality, which explains the discrepancies reported in the literature and the large difference measured in this work with deposited samples less influenced by GeO formation and irradiation damage.

C. Co-implantation of Si

To control the diffusion and position of germanium atoms after annealing, we take advantage of the Si/Ge trapping effect explained above. $^{29}Si^+$ and $^{30}Si^-$ isotopes were implanted on either side of the Ge depth-distribution prior to the thermal annealing to act as a diffusion barrier for Ge.[5,13–15] Figure 4 illustrates the depth-profiles of five samples implanted with Ge at a fluence of

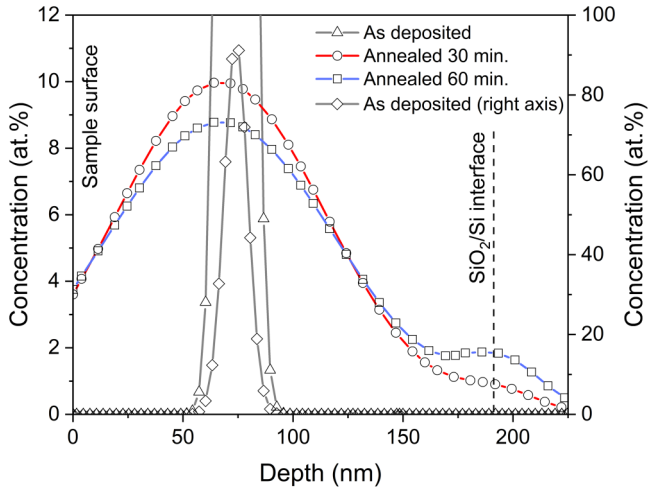

FIG. 3. Ge depth-profiles (RBS) of deposited samples (SiO_2/Ge/SiO_2) before and after 30 and 60 min annealing at 1100 °C under a pure N_2 atmosphere.

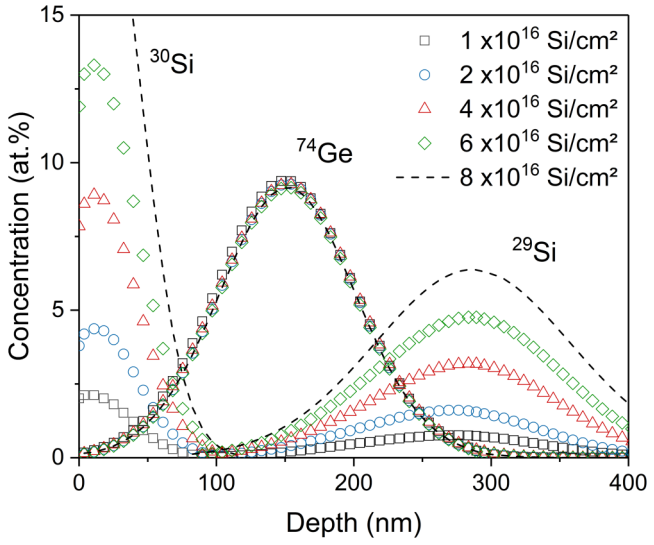

FIG. 4. ^{74}Ge, ^{29}Si, and ^{30}Si depth-profiles (curves used to fit RBS/RNRA data), measured by RBS/RNRA, of co-implanted samples for fluences varying from 1 to 6 × 10^{16} Si/cm^2. The implantation sequence permits to obtain the same Ge depth-profile for each sample with different overlaps when the ^{30}Si and ^{29}Si fluences increase.

8×10^{16} ^{74}Ge/cm^2 and co-implanted at silicon fluences ranging from 1×10^{16} to 8×10^{16} Si/cm^2, as measured by RBS. Although the central positions of the Si depth-distribution may vary from several nanometers with the ion fluences due to ion erosion,[16] the silicon excess introduced by ion implantation into the samples is basically localized between the first 100 nm of the sample for ^{30}Si and deeper than 100 nm for ^{29}Si. As the silicon diffusion is negligible compared to that of germanium,[6] the depth-profiles of co-implanted Si remain unchanged after thermal treatment. For each co-implanted sample, no germanium losses are measured after annealing within the accuracy limits of the RBS technique. As shown by the Ge depth-profiles presented in Fig. 5, the germanium diffusion is completely stopped for Si co-implanted fluences greater than 2×10^{16} Si/cm^2. This shows that, as for the upward diffusion,[5] the in-depth diffusion of Ge can be blocked using Si co-implantation. The value at which the diffusion barrier effects become optimal on RBS profiles corresponds to a maximum Si excess atom concentration of about 4.5 at. % and 1.6 at. % for low and high energies of implantation, respectively. Such a density is very low compared to the one previously reported in fused silica, where each co-implanted Si atom is found to block one diffusing Ge on average.[14] We infer that the need for a smaller amount of Si excess to stop the diffusion of Ge in the SiO_2/Si samples is due to the higher concentration of silicon dangling bonds, whose presence within the thermal oxide also contributes to the Si/Ge trapping via the formation of Ge–Si chemical bonds.[5,11]

Under 2×10^{16} Si/cm^2, diffusion in both directions appears to be the dominant regime. The excess of co-implanted silicon is not sufficient, and the diffusion process is marked upward and ruled the same way than for not co-implanted samples shown in Fig. 2.

A configuration without the low energy implantation at 35 keV has been tested to highlight the in-depth blocking and the potential effect on upward diffusion. The ^{29}Si$^+$ implantation at 170 keV was replaced by ^{30}Si$^+$ because of a resonance more intense by a factor 2.5. Two samples implanted with measured fluences of 1.2×10^{17} ^{74}Ge/cm^2, co-implanted with 2 and 6×10^{16} ^{30}Si/cm^2, respectively, were annealed at 1100 °C during 1 h. Figure 6 shows a completely annihilated Ge diffusion in regions where Si excess was co-implanted, while Ge upward diffusion dominates in the 70–85 first nanometers (depending on the ^{30}Si fluence) where no Si excess has been implanted. A fluence-dependent effect is observed due to surface erosion and the increased density of damage with the fluence. The high energy implantation is not sufficient to block upward diffusion in the subsurface region even for a fluence of 6×10^{16} ^{30}Si/cm^2, corresponding to a local concentration of 4.5 at. %. This confirms the strong upward diffusion of Ge in regions not co-implanted with Si excess and the importance of co-implanted Si as a barrier for Ge diffusion. ^{30}Si induced-defects are distributed throughout the Ge profile, as well as damage induced by ^{74}Ge due to surface erosion (~15 nm), as calculated by TRIM. Damage contribution is less significant due to matrix restoration occurring during annealing. This additional result is consistent with an upward diffusion of Ge annihilated by the formation of Si/Ge chemical bonds due to co-implanted Si and irradiation defects.

D. Nanoclustering

In order to bring out the role of each silicon isotope, μ-Raman analyses have been performed. Figure 7 shows the Raman signature of Ge implanted samples co-implanted with ^{30}Si$^-$ and ^{29}Si$^+$ after

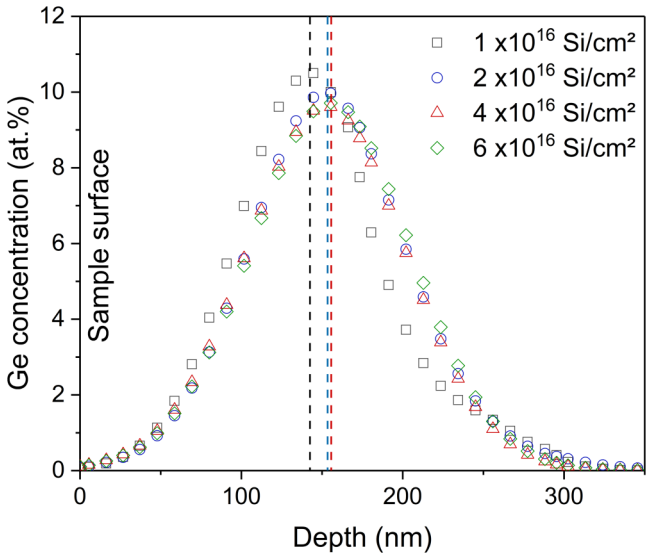

FIG. 5. Concentration of ^{74}Ge after 1 h annealing at 1100 °C under an N_2 atmosphere for samples co-implanted with fluences varying from 1 to 6×10^{16} Si/cm^2 (fitted from RBS/RNRA spectra).

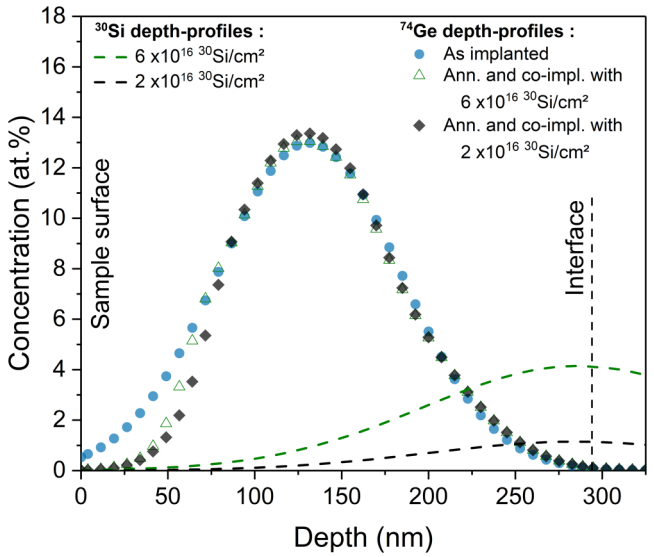

FIG. 6. Fitting curves of the RBS/RNRA analysis of 8×10^{16} ^{74}Ge/cm^2 co-implanted with 2 and 6×10^{16} ^{30}Si/cm^2. ^{30}Si is implanted at 170 keV to annihilate the in-depth diffusion of Ge.

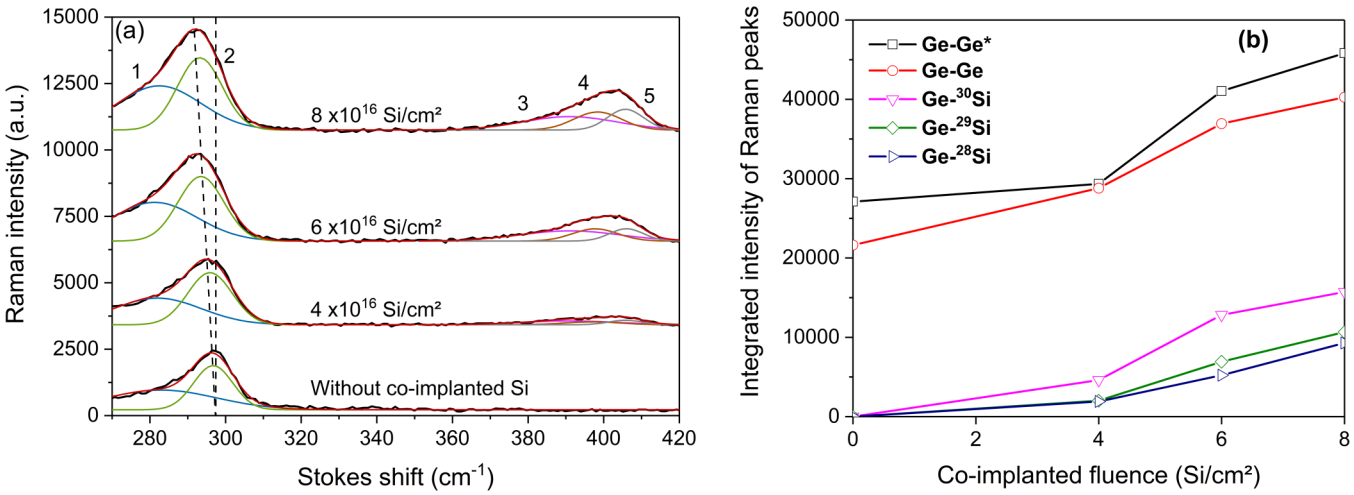

FIG. 7. μ-Raman spectra of samples co-implanted with 4, 6, and 8×10^{16} Si/cm^2 and without Si (a) and integrated intensity of Raman peaks (b).

1 h annealing at 1100 °C. The spectral range of 270–420 cm^{-1} was chosen to eliminate the strong contribution of the TO phonon mode of the Si substrate around 520 cm^{-1} and to zoom on the region where Raman phonons related to Ge-ncs and Ge/Si clusters appear.[14] In agreement with previous studies,[5,13,20–26] peaks 1 and 2 observed at 280 and 295 cm^{-1} in Fig. 7(a) are associated with the signature of Ge nanocrystals containing Si impurities and pure Ge nanocrystals, respectively. The increase of peak 1 with the increase of the co-implanted Si fluence supports this assignation. Ge–Si phonons peaks, around 400 cm^{-1}, are the phonons related to the formation of ^{30}Si-Ge (peak 3), ^{29}Si-Ge (peak 4), and ^{28}Si-Ge (peak 5) bonds. Their positions of 391, 398, and 406 cm^{-1} were maintained constant during spectral deconvolution and correspond to the wavenumbers calculated for isotopic effect using the $M^{-1/2}$ dependence of the phonon frequency.[26]

While the contributions of co-implanted Si for ion fluences lower 4×10^{16} Si/cm^2 are below the μ-Raman detection limit, both the signals related to the Ge nanoclusters and the Si/Ge aggregates are found to increase with the increase of the ^{30}Si and ^{29}Si concentrations. This trend is consistent with the reduction of the thermal diffusion of Ge throughout the whole SiO_2 matrix shown in Fig. 5 and discussed in Sec. IV C, which promotes the clustering of Ge within the region where the concentration of implanted Ge is the highest.

The presence of the two Ge–^{30}Si and Ge–^{29}Si Raman peaks confirm that silicon excess participates actively to the blocking of implanted germanium atoms. The evolution of Ge–^{30}Si, Ge–^{29}Si, and Ge–^{28}Si peaks is presented in Fig. 7(b), indicating that the formation of Si/Ge clusters is dominated by the formation of Ge–^{30}Si bonds. As the intensity of the phonon Raman peaks is usually proportional to the density of chemical bonds related to this vibration, such a feature would be a direct consequence of the preponderant Ge upward diffusion, through the formation of GeO. This result is supported by RBS measurements, shown in Fig. 2 that a majority of Ge diffuses toward the sample surface, where the presence of ^{30}Si excess in co-implanted samples promotes locally its trapping. Such a feature is further pronounced by the fact that according to the overlap of the ^{30}Si/Ge and ^{29}Si/Ge depth-distribution, evaluated from the RBS spectra of Fig. 4 and reported in Fig. 8, the quantity of co-implanted Si introduced into the Ge-implanted region is nominally greater for ^{29}Si than for ^{30}Si. Due to ion erosion, this overlap increases with the fluence of co-implanted Si. In Fig. 8, the relative spatial superposition of the Ge–^{30}Si/Ge–^{29}Si depth-profiles is about 0.50 for a co-implantation at 8×10^{16} Si/cm^2, while the

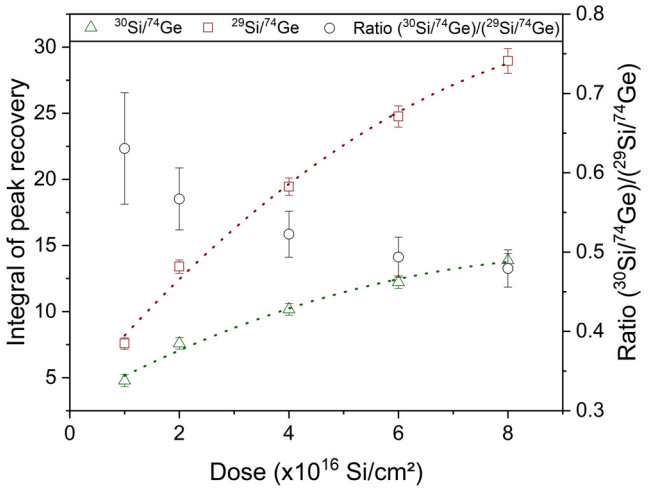

FIG. 8. ^{29}Si/^{74}Ge (□) and ^{30}Si/^{74}Ge (Δ) profiles overlapping measured by RBS (deduced from Fig. 4). The overlap ratio (o) decreases due to a faster increase of ^{29}Si/^{74}Ge compared to ^{30}Si/^{74}Ge.

concentration of Ge–^{30}Si bonds found by μ-Raman in Fig. 7(b) still remains 50% higher than that of Ge–^{29}Si bonds. This confirms that even if there are more ^{29}Si in the surrounding of implanted Ge, the formation of Ge–^{30}Si in the first 50 nm of the samples still dominates due to the greater upward diffusion of Ge.

The increase of the Ge–^{28}Si Raman peak with co-implantation fluence suggests a "kick-out" effect generated by the implanted species: a fraction of implanted Si can substitute to ^{28}Si atoms in the SiO_2 matrix, inducing an increase of ^{28}Si excess through the dioxide layer.

The influence of Si co-implantation on Ge nanocrystal size and purity has been investigated by TEM and discussed in Refs. 5 and 14. The more the Si fluence is increasing, the more the Ge-ncs diameter is reducing due to the decrease of Ge thermal diffusion, which is consistent with the current results. As a consequence, the concentration of co-implanted Si can be set to control the size of the formed nanocrystals and their distribution over the SiO_2 layer. In addition, samples co-implanted with Si were found to contain Ge-ncs with interplanar spacings 2%–3% smaller than that of not co-implanted samples.[5] These two features contribute to both the redshift[35] and the spectral broadening of the Ge-nc Raman peak in agreement with our measurements.

V. CONCLUSIONS

RBS/RNRA investigations showed that the thermally activated diffusion of Ge atoms implanted in the middle of an SiO_2/Si layer occurs upward (surface) and downward (interface). This diffusion is asymmetric due to the formation of highly volatile GeO, which favors out-diffusion. It is brought out that low quantities of co-implanted Si excess (from 2×10^{16} Si/cm^2, corresponding to 4.5 at. % at low energy and 1.6 at. % at high energy), implanted on either side of Ge, are sufficient to completely annihilate Ge diffusion in both directions for a Ge fluence of 8×10^{16} ^{74}Ge/cm^2 (10 at. % at maximum). Silicon isotopes were used in order to highlight the contribution of the two Si implantations, with ^{30}Si and ^{29}Si implanted at 35 and 170 keV, respectively. Upward diffusion observed by RBS was confirmed by μ-Raman analyses systematically presenting a larger density of Ge–^{30}Si chemical bonds. μ-Raman analysis showed the importance of co-implantation of Si excess in Si/Ge trapping and nanoclustering by measuring a dependence, as a function of the fluence of co-implanted Si, on the density of Ge–^{30}Si and Ge–^{29}Si bonds.

The important role of implantation-induced defects has been highlighted using a deposited sample free of irradiation damage. In the absence of implantation, Ge diffusion is less limited by the density of defects and a coefficient of diffusion as high as $D_{1100°C} \sim 10^{-14}$ cm^2/s is found. This value is two orders of magnitude higher than coefficients generally measured for implanted samples due to structural differences of the SiO_2 layer and the absence of implantation-induced defects. Deposition also prevents GeO formation, responsible for upward diffusion, resulting in symmetric Ge diffusion in both directions.

ACKNOWLEDGMENTS

This work was supported by the Québec-Wallonie-Bruxelles collaboration (RECH-INNO-02). The authors would like to thank I. Vickridge for his advice during our discussions, T. Tabarrant for the technical support on the ALTAÏS accelerator, and the SIAM (Synthesis, Irradiation and Analysis of Materials) technological platform of the University of Namur. D.B. would like to thank the 9e Commission mixte permanente Québec/Wallonie-Bruxelles of MRIF for supporting this collaboration.

DATA AVAILABILITY

The data that support the findings of this study are available from the corresponding author upon reasonable request.

REFERENCES

[1]M. A. Green and S. P. Bremner, Nat. Mater. **16**, 23 (2017).
[2]M. Yedji, J. Demarche, G. Terwagne, R. Delamare, D. Flandre, D. Barba, D. Koshel, and G. G. Ross, J. Appl. Phys. **109**, 084337 (2011).
[3]M. C. Beard, K. P. Knutsen, P. Yu, J. M. Luther, Q. Song, W. K. Metzger, R. J. Ellingson, and A. J. Nozik, Nano Lett. **7**, 2506 (2007).
[4]M. T. Trinh, R. Limpens, W. D. A. M. de Boer, J. M. Schins, L. D. A. Siebbeles, and T. Gregorkiewicz, Nat. Photonics **6**, 316 (2012).
[5]D. Barba, C. Wang, A. Nélis, G. Terwagne, and F. Rosei, J. Appl. Phys. **123**, 161540 (2018).
[6]M. V. Minke and K. A. Jackson, J. Non-Cryst. Solids **351**, 2310 (2005).
[7]A. Markwitz, B. Schmidt, W. Matz, R. Grötzschel, and A. Mücklich, Nucl. Instr. Meth. B **142**, 338 (1998).
[8]V. Beyer and J. von Borany, Phys. Rev. B **77**, 014107 (2008).
[9]D. Barba, F. Martin, J. Demarche, G. Terwagne, and G. G. Ross, Nanotechnology **23**, 145701 (2012).
[10]C. Li, H. Feng, B. Liu, W. Liang, G. Liu, G. G. Ross, Y. Wang, and D. Barba, Nanotechnology **28**, 035707 (2017).
[11]D. Barba, R. Cai, J. Demarche, Y. Wang, G. Terwagne, F. Rosei, F. Martin, and G. G. Ross, Appl. Phys. Lett. **104**, 111901 (2014).
[12]K. H. Heinig, B. Schmidt, A. Markwitz, R. Grötzschel, M. Strobel, and S. Oswald, Nucl. Instrum. Methods Phys. Res. B **148**, 969 (1999).
[13]D. Barba, J. Demarche, F. Martin, G. Terwagne, and G. G. Ross, Appl. Phys. Lett. **101**, 143107 (2012).
[14]D. Barba, F. Martin, J. Demarche, G. Terwagne, and G. G. Ross, J. Appl. Phys. **114**, 074306 (2013).
[15]R. S. Cai, Y. Q. Wang, L. Shang, X. H. Liu, Y. J. Zhang, G. G. Ross, and D. Barba, J. Appl. Phys. **115**, 204310 (2014).
[16]J. F. Ziegler, M. D. Ziegler, and J. P. Biersack, Nucl. Instrum. Methods Phys. Res. B **268**, 1818 (2010).
[17]G. Amsel, E. d'Artemare, G. Battistig, E. Girard, L. G. Gosset, and P. Révész, Nucl. Instrum. Methods Phys. Res. B **136–138**, 545 (1998).
[18]V. Baranwal, J. W. Gerlach, A. Lotnyk, B. Rauschenbach, H. Karl, S. Ojha, D. K. Avasthi, D. Kanjilal, and A. C. Pandey, J. Appl. Phys. **118**, 134303 (2015).
[19]J. von Borany, R. Grötzschel, K. H. Heinig, A. Markwitz, W. Matz, B. Schmidt, and W. Skorupa, Appl. Phys. Lett. **71**, 3215 (1997).
[20]A. Rodríguez, M. I. Ortiz, J. Sangrador, T. Rodríguez, M. Avella, A. C. Prieto, A. Torres, J. Jiménez, A. Kling, and B. C. Ballesteros, Nanotechnology **18**, 065702 (2007).
[21]O. Pagès, J. Souhabi, V. J. B. Torres, A. V. Postnikov, and K. C. Rustagi, Phys. Rev. B **86**, 045201 (2012).
[22]A. S. Vasin, O. V. Vikhrova, and M. I. Vasilevskiy, J. Appl. Phys. **115**, 143505 (2014).
[23]L. Z. Liu, F. Gao, X. L. Wu, T. H. Li, and P. K. Chu, Appl. Phys. Lett. **95**, 171105 (2009).
[24]A. Rodríguez, T. Rodríguez, A. C. Prieto, J. Jiménez, A. Kling, C. Ballesteros, and J. Sangrador, J. Electon. Mater. **39**, 1194 (2010).
[25]D. Barba, D. Koshel, F. Martin, G. G. Ross, M. Chicoine, F. Schiettekatte, M. Yedji, J. Demarche, and G. Terwagne, J. Lum. **130**, 669 (2010).
[26]M. Cardona, Phys. Status Solidi B **220**, 5 (2000).

[27]S. Oswald, B. Schmidt, and K. H. Heinig, Surf. Interface Anal. **29**, 249–254 (2000).
[28]G. Deconninck and B. Van Oystaeyen, Nucl. Instrum. Methods Phys. Res. B **218**, 165–170 (1983).
[29]M. Mayer, "SIMNRA, a simulation program for the analysis of NRA, RBS and ERDA," AIP Conf. Proc. **475**, 541 (1999).
[30]C. Jeynes, N. P. Barradas, P. K. Marriott, G. Boudreault, M. Jenkin, E. Wendler, and R. P. Webb, J. Phys. D: Appl. Phys. **36**, R97 (2003).
[31]I. Vickridge, Curr. Appl. Phys. **3**, 51–55 (2003).
[32]Y. Wang and M. Nastasi, *Handbook of Modern Ion Beam Materials Analysis*, 2nd ed. (Materials Research Society, 2009).
[33]X. Hao *et al.*, J. Nanosci. Nanotechnol. **8**, 1350–1354 (2008).
[34]Y. Takakuwa *et al.*, Jpn. J. Appl. Phys. **32**, L480–L483 (1993).
[35]I. Doğan and M. C. M. van de Sanden, J. Appl. Phys. **114**, 134310 (2013).
[36]J. L. Colaux, "Characterisation of carbon nitride compounds synthesized by simultaneous implantation of carbon and nitrogen in copper," doctoral dissertation (University of Namur, 2009).
[37]G. Terwagne, M. Piette, and F. Bodart, Nucl. Instrum. Methods Phys. Res. B **19–20**, 145–149 (1987).
[38]S. Lucas, F. Bodart, G. Terwagne, G. Sorensen, and H. Jensen, Mater. Sci. Eng. B **2**, 183–187 (1989).